Analysis and Improvement of Tipping Calibration for Ground-Based Microwave Radiometers

Yong Han and Ed R. Westwater, *Senior Member, IEEE*

***Abstract*—The tipping-curve calibration method has been an important calibration technique for ground-based microwave radiometers that measure atmospheric emission at low optical depth. The method calibrates a radiometer system using data taken by the radiometer at two or more viewing angles in the atmosphere. In this method, the relationship between atmospheric opacity and viewing angle is used as a constraint for deriving the system calibration response. Because this method couples the system with radiative transfer theory and atmospheric conditions, evaluations of its performance have been difficult. In this paper, first a data-simulation approach is taken to isolate and analyze those influential factors in the calibration process and effective techniques are developed to reduce calibration uncertainties. Then, these techniques are applied to experimental data.**

The influential factors include radiometer antenna beam width, radiometer pointing error, mean radiating temperature error, and horizontal inhomogeneity in the atmosphere, as well as some other factors of minor importance. It is demonstrated that calibration uncertainties from these error sources can be large and unacceptable. Fortunately, it was found that by using the techniques reported here, the calibration uncertainties can be largely reduced or avoided. With the suggested corrections, the tipping calibration method can provide absolute accuracy of about or better than 0.5 K.

***Index Terms*—Calibration, ground-based, microwave radiometers.**

I. Introduction

DUE TO recent emphasis on the application of line-by-line radiative transfer models (LBLRTM) to climate models [1] and to assimilation of satellite data in weather forecasting [2], the accuracy of forward models to calculate absorption and emission spectra during clear sky conditions is of increasing importance. Measurement of water vapor profiles is fundamental to these and to many other atmospheric and climate problems. With the increasing deployment of Fourier transform interferometric radiometers (FTIR) [3], [4] at observation sites around the world, an excellent data base of well-calibrated radiance data is becoming available through the U. S. Department of Energy's Atmospheric Radiation Measurement (ARM) program [5]. The conventional way of evaluating and improving models is to measure vertical profiles of temperature and relevant emitting constituents, use these measurements as input to LBLRTM, and compare measured and calculated radiance.

Manuscript received January 20, 1999; revised July 20, 1999. This work was supported by the U. S. Department of Energy, Environmental Sciences Division, Atmospheric Radiation Measurement Program, Washington, DC.

The authors are with the Cooperative Institute for Research in Environmental Sciences (CIRES), University of Colorado/NOAA, Environmental Technology Laboratory, Boulder, CO 80303-3228 USA (e-mail: yhan@etl.noaa.gov).

Publisher Item Identifier S 0196-2892(00)02481-5.

A limiting factor in evaluating LBLRTM is the accuracy of the humidity profiles used as input to the model. Research reported by Liljegren and Lesht [6] showed that there were substantial differences between relative-humidity sensors on radiosondes that were obtained from different calibration lots (i.e., batches of radiosondes that were calibrated at different times). Thus, a limiting factor in evaluating LBLRTM is the accuracy of the humidity profiles used as input to the model. Recognizing the need to overcome this limitation, two water vapor intensive operating periods (WVIOP) were conducted at the ARM cloud and radiation testbed (CART) site in 1996 and 1997. This paper focuses on the 1997 observations obtained at or near the ARM Southern Great Plains (SGP) central facility (CF) near Lamont, OK [5]. A primary goal of these experiments was the comparison of the absolute accuracy of both remote and *in situ* humidity sensors.

Ground-based microwave radiometers (MWR) have been widely used to measure atmospheric water vapor and cloud liquid water. Frequencies on the 22.235 GHz water vapor absorption band and in the 31 GHz absorption window region are commonly used in the systems. These frequency channels differentiate in their response to water vapor and cloud liquid water and provide brightness temperature measurements from which precipitable water vapor (PWV) and integrated cloud liquid water (ICL), as well as low-vertical-resolution water vapor profiles, are derived [7]–[9]. The absolute calibration is fundamental in determining the accuracies of these retrievals, although some other factors are important as well [10]. For a dual-channel radiometer at 23.8 and 31.4 GHz, 1° calibration error may cause about 1 mm error in PWV.

The importance of the PWV measurements and thus, the importance of the system calibration, has increased in recent years as the MWR measurements are often served as references and comparison standards for other water vapor measuring instruments, such as radiosondes, Raman water vapor lidars, and global positioning systems (GPS) [11]. Part of the motivation for the WVIOP's was the suggestion by Clough *et al*. [12] that MWR measurements of PWV could be used to scale radiosonde observations to more realistic values. The possibility also exists for using the MWR or the GPS to help calibrate Raman lidar measurements of mixing ratio profiles. Such a referencing role has been played recently at the Department of Energy's ARM CART CF site. It has been observed at the site that the spectra measured by an FTIR are closer to the results from the LBLRTM that uses radiosonde water vapor profiles scaled by the PWV from the MWR than those from the LBLRTM without using the scaling [12].

From September 15 to October 5, 1997, WVIOP'97 was conducted at the ARM CART site. During WVIOP'97, the

U.S. Government work not protected by U.S. copyright

Authorized licensed use limited to: Susanne Crewell. Downloaded on March 29, 2009 at 09:05 from IEEE Xplore. Restrictions apply.

NOAA's Environmental Technology Laboratory (ETL) operated two microwave radiometers at the CART site. During the same time, NOAA's forecast systems laboratory (FSL) operated two GPS's, one at the SGP CF and one at NOAA's wind profiler site near Lamont, OK, about 9 km away from the CF. NASA's Goddard Space Flight Center (NASA/GDFC), Greenbelt, MD, operated a Raman water vapor lidar, and the ARM operational Raman lidar was operated as well. At the CF, ARM has also routinely operated an MWR for several years [7]. The primary goal of these deployments was to quantify the absolute accuracies of the MWR's and GPS's in PWV and to compare these measurements with *in situ* measurements made every 3 h by ARM's balloon borne sounding systems (BBSS). Preliminary intercomparisons among these instruments showed that the PWV from the ARM's MWR was consistently higher than that from all other instruments. With other instruments being in agreement with one another, a logical step was to examine the calibration process performed on both ARM and ETL MWR's during the experiment. This led to the investigation of the calibration method that we present here.

Microwave radiometers that are used in space are usually calibrated using known calibration reference targets [13]. However, it is desirable to have a target temperature close to the brightness temperatures that an MWR measures during regular observations. For the upward-looking radiometer channels considered here, the observed brightness temperature can be as low as 10 K. Two calibration methods are often applied for these channels: using a liquid nitrogen LN_2-cooled blackbody target or a tipping calibration method that uses a clear atmosphere as a calibration reference. If applied with care and caution, the LN_2 method can be useful. However, it is not practical to be applied and automated in long-term, routine operations. With the tipping method [14], [15], the radiometer takes measurements at two or more elevation angles in a horizontally-stratified atmosphere. The calibration is accomplished by adjusting a single numerical calibration parameter that is required by the system software until the outputs of the system comply with a known physical relationship. In addition, as discussed in Section IV-G, strict quality control methods must also be applied to the data before the calibration parameter is changed. With suitable scanning, the calibration procedure can be automated. The ETL's and ARM's radiometer systems were all calibrated using the tipping calibration method during the experiment.

The tipping method couples a radiometer equation that is specific to the radiometer in use and the theory of the radiative transfer in the atmosphere. Calibration uncertainties may arise from both the system and the application of the theory. To investigate and reduce the uncertainties, we first take a simulation approach to reveal problems and develop techniques to solve them. We then apply these techniques to the data taken during WVIOP'97. The simulations are based on radiosonde data collected around the area of the CART site. Although the data are site specific, results of the analysis are general, and the techniques developed can be applied to all tipping calibrations.

II. Radiative Transfer and Radiometer Equations

The fundamental quantity a radiometer measures is radiation power, which is related to the specific intensity (or radiance) I_ν, defined as the radiation power per unit area, per unit frequency interval at a specified frequency ν, and per unit solid angle at a specified direction. However, in the microwave frequency region, the intensity is usually expressed as brightness temperature, denoted as $T_{b,\nu}$. In microwave radiometry, there are two popular definitions of the brightness temperature. Because of the differences between these two difinitions, some confusion and mistakes may arise when measurements or models are compared. Because it is important to be aware of the issue, we include a brief discussion in the following. A detailed discussion is given in Janssen [16] and Stogryn [17].

The so-called Rayleigh–Jeans equivalent brightness temperature is defined as

$$T_{b,\nu}^{(\mathrm{RJE})} = \frac{c^2}{2\nu^2 k} I_\nu \tag{1}$$

where c, k, and ν are the speed of light, Boltzmann's constant, and frequency, respectively. Note that (1) is not the traditional Rayleigh–Jeans approximation. $T_{b,\nu}^{(\mathrm{RJE})}$ is a scaled intensity in temperature units. The second definition is the so-called thermodynamic brightness temperature, defined as

$$T_{b,\nu}^{(\mathrm{TRM})} = B_\nu^{-1}(I_\nu) \tag{2}$$

where B_ν^{-1} is the inverse of the Planck function $B_\nu(T_{b,\nu})$ at a temperature $T_{b,\nu}$. The Planck function $B_\nu(T)$ is the radiance emitted at ν from a blackbody at temperature T and is given by

$$B_\nu(T) = \frac{2h\nu^3}{c^2} \frac{1}{\exp\left(\dfrac{h\nu}{kT}\right) - 1}. \tag{3}$$

By way of analogy, $T_{b,\nu}^{(\mathrm{TRM})}$ is an equivalent temperature at which a blackbody emits the amount of radiation at the intensity I_ν. The conversion from $T_{b,\nu}^{(\mathrm{TRM})}$ to $T_{b,\nu}^{(\mathrm{RJE})}$ is

$$T_{b,\nu}^{(\mathrm{RJE})} = \frac{c^2}{2\nu^2 k} B_\nu\left(T_{b,\nu}^{(\mathrm{TRM})}\right). \tag{4}$$

Unlike $T_{b,\nu}^{(\mathrm{RJE})}$, $T_{b,\nu}^{(\mathrm{TRM})}$ is not linearly related to I_ν. Expanding the Planck function B_ν in terms of $h\nu/kT_{b,\nu}$, one obtains

$$\frac{c^2}{2\nu^2 k} I_\nu = T_{b,\nu}^{(\mathrm{RJE})} = T_{b,\nu}^{(\mathrm{TRM})} - \frac{h\nu}{2k} + \frac{h^2\nu^2}{12k^2 T_{b,\nu}^{(\mathrm{TRM})}} + \cdots \tag{5}$$

where h is the Planck constant. The first term is the traditional Rayleigh–Jeans approximation, and the second may be considered at a first-order correction to the Rayleigh–Jeans approximation and depends not on $T_{b,\nu}^{(\mathrm{TRM})}$, but only on frequency. In the region $\nu < 300$ GHz, the first two terms are usually sufficient for applications, except when $T_{b,\nu}^{(\mathrm{TRM})}$, is very low (e.g., for the cosmic background at 2.75 K). Thus, under normal conditions, for the amount of radiation received by ground-based radiometers, the difference between $T_{b,\nu}^{(\mathrm{RJE})}$ and $T_{b,\nu}^{(\mathrm{TRM})}$ is well represented by the second term in (5), $h\nu/2k$, which is proportional to frequency. At 20.6 GHz, this term has a value of 0.49 K and 31.4 GHz, a value of 0.75 K. Even when $T_{b,\nu}^{(\mathrm{TRM})}$ is as low as the cosmic background at 2.75 K, the sum of the remaining terms is not significant for the frequencies considered here. For example, for $T_{b,\nu}^{(\mathrm{TRM})} = 2.75$ K, the third term is equal to 0.030 K at 20.6 GHz and 0.069 K at 31.4 GHz. However, it may be significant at higher frequencies.

Authorized licensed use limited to: Susanne Crewell. Downloaded on March 29, 2009 at 09:05 from IEEE Xplore. Restrictions apply.

Following Janssen [16], the definition of $T_{b,\nu}^{(\mathrm{RJE})}$ may be applied to scale the uplooking radiative transfer equation

$$I_\nu = I_{bb,\nu} e^{-\tau_\nu(\infty)} + \int_0^{\tau_\nu(\infty)} B_\nu(T) e^{-\tau_\nu}\, d\tau_\nu \tag{6}$$

into an equation with temperature units as

$$T_{b,\nu}^{(\mathrm{RJE})} = T_{bb,\nu}^{(\mathrm{RJE})} e^{-\tau_\nu(\infty)} + \int_0^{\tau_\nu(\infty)} T'_\nu e^{-\tau_\nu}\, d\tau_\nu \tag{7}$$

where $T_{bb,\nu}^{(\mathrm{RJE})}$ is the cosmic background temperature and is a function of fequency, and T'_ν is defined as

$$T'_\nu = \frac{B_\nu(T)c^2}{2\nu^2 k}. \tag{8}$$

Note that T'_ν is not equal to the physical air temperature T.

The radiometer equation relates the system output voltage to input radiation power. Usually, an MWR system views one or more internal or external blackbody targets for initial calibrations. Taking a simple example, if a linear system has two calibration reference targets at temperatures T_1 and T_2, the intensity I_ν (averaged over an antenna beam) measured by the radiometer observing the sky, may be given by the following radiometer equation

$$I_\nu = (B_\nu(T_2) - B_\nu(T_1))(V_s - V_1)/(V_2 - V_1) + B_\nu(T_1) \tag{9}$$

where V_s, V_1, and V_2 are detected voltages from the sources of the sky, target 1, and target 2, respectively. The radiometer equation may be scaled in the same way as that for obtaining the radiative transfer (7). Thus, the measurements given by the scaled radiometer equation are consistent with the radiative transfer equation (7). Note that in the scaled equation, the quantities $c^2 B_\nu(T)/2\nu^2 k$ ($T = T_1$ or T_2) are not equal to T_1 or T_2.

It is common, however, that physical temperatures are directly used in the radiometer equations. This is done by linearizing $B_\nu(T)$ in terms of T (i.e., using the first two terms in the expansion similar to (5)). If we substitute each of the radiation intensities, $I_\nu = aT_{b,\nu}^{(\mathrm{TRM})} - \Delta$, $B_\nu(T_1) = aT_1 - \Delta$, and $B_\nu(T_2) = aT_2 - \Delta$, where $a = 2\nu^2 k/c^2$ and $\Delta = h\nu^3/c^2$ into (9), we have

$$T_{b,\nu}^{\mathrm{TRM}} = (T_2 - T_1)(V_s - V_1)/(V_2 - V_1) + T_1. \tag{10}$$

We see that this radiometer equation is consistent with the model that computes the thermodynamic brightness temperature $T_{b,\nu}^{(\mathrm{TRM})}$ but is not consistent with the radiative transfer (7) that calculates $T_{b,\nu}^{(\mathrm{RJE})}$. As discussed earlier, under normal conditions, (10) is sufficient for applications. However, in situations such as zenith radiometric observations from aircraft, the atmospheric radiation power may be too low to be linearized in terms of the thermodynamic temperature and thus, the radiometer (10) may not be valid.

In many applications of ground-based radiometry, including tipping calibrations, there is a need to map the atmospheric radiation power into optical depth or opacity. This can be achieved after defining a mean radiating temperature based on the radiative transfer equation (7)

$$T_{mr,\nu}^{(\mathrm{RJE})}(\theta) = \int_0^\infty T'_\nu e^{-\tau_\nu(\theta)}\, d\tau_\nu(\theta) \Big/ \left(1 - e^{-\tau_\nu(\infty,\theta)}\right) \tag{11}$$

where $\tau_\nu(\theta)$ is the optical path, and $\tau_\nu(\infty, \theta)$ is the opacity at an elevation angle θ. The opacity is then calculated as [for convenience, we will drop the symbol ∞ and express the opacity as $\tau_\nu(\theta)$]

$$\tau_\nu(\theta) = \ln\left(\frac{T_{mr,\nu}^{(\mathrm{RJE})}(\theta) - T_{bb,\nu}^{(\mathrm{RJE})}}{T_{mr,\nu}^{(\mathrm{RJE})}(\theta) - T_b^{(\mathrm{RJE})}(\theta)}\right). \tag{12}$$

Note that in (12), the sky brightness temperature is defined as that of the Rayleigh–Jeans equivalent $T_{b,\nu}^{(\mathrm{RJE})}$ using (4) because it is defined as a thermodynamic brightness temperature. If we express each of the quantities in (12) in terms of the temperatures given by (4) and expand the Planck functions, we may calculate the opacity as

$$\tau_\nu(\theta) = \ln\left(\frac{T_{mr,\nu}^{(\mathrm{TRM})}(\theta) - T_{bb,\nu}^{(\mathrm{TRM})}}{T_{mr,\nu}^{(\mathrm{TRM})}(\theta) - T_{b,\nu}^{(\mathrm{TRM})}(\theta)}\right) \tag{13}$$

after neglecting the third and higher terms, where

$$\begin{aligned} T_{mr,\nu}^{(\mathrm{TRM})}(\theta) &= B_\nu^{-1}\left(\int_0^\infty B_\nu(T) e^{-\tau_\nu(\theta)}\, d\tau_\nu(\theta) \Big/ \left(1 - e^{-\tau_\nu(\theta,\infty)}\right)\right) \\ &= B_\nu^{-1}\left(\frac{2\nu^2 k}{c^2} T_{mr,\nu}^{(\mathrm{RJE})}(\theta)\right). \end{aligned} \tag{14}$$

In (13), $T_b^{(\mathrm{TRM})}$ may be substituted with the measurements given by (10) directly. However, since (13) is an approximation of the exact (12), we should caution on the treatment of the quantity representing the cosmic background or sky brightness temperature with very low value. In some applications, neglecting the third term may not be valid.

When mapping the measurements to opacity, it is important that the parameters in the mapping function be consistent with the radiometer equation. For example, if the cosmic background is given in Rayleigh–Jeans equivalent brightness temperature, and the sky temperature is given in thermodynamic brightness temperature, an inconsistency occurs that will fold a bias of 0.75 K at 31.4 GHz into the calculation of opacity.

The tipping calibration method is usually applied to determine the values of some constants in the radiometer equation that models an MWR system's input–output relationship. We assume the MWR systems are linear and characterized by two constants such as a system gain and an offset [18]. If accurate calibration reference targets are available at two temperatures that span the range of observable brightness temperatures, then the two constants can be determined. In many cases, the systems have partial calibration information, with one of the constants approximately known, and leave the other to be determined in the calibration processes. For example, the ETL radiometers have two internal calibration references, but the transmission by a window and a segment of a waveguide need to be determined. In the following (and thereafter), we use the ETL's and ARM's systems as examples to illustrate the tipping calibration analysis. The results are general for other types of radiometers.

Each of the two ETL systems contains two independent microwave radiometers: one operates at 20.6 or 23.87 GHz and the other at 31.65 GHz. Other system parameters are listed in Table

Authorized licensed use limited to: Susanne Crewell. Downloaded on March 29, 2009 at 09:05 from IEEE Xplore. Restrictions apply.

TABLE I
SELECTED RADIOMETER PARAMETERS: FREQUENCY (GHz), BANDWIDTH (GHz), $\theta_{1/2}$–FULL WIDTH AT HALF-MAXIMUM POWER OF THE ANTENNA PATTERN (DEGREES)

	ETL-1		ETL-2		ARM	
Frequency	20.6	31.65	23.87	31.65	23.8	31.4
Bandwidth	0.5	0.5	0.5	0.5	0.4	0.4
$\theta_{1/2}$	4.0	4.0	4.0	4.0	5.7	4.0

I. Each radiometer has two internal blackbody loads, one at temperature T_r, near 300 K, and the other at T_h, about 100 K higher than T_r. The radiometer equation of the system is given as [14]

$$T_{A,m} = c\left(\frac{T_h - T_r}{V_h - V_r}(V_s - V_r) + T_r - T_w\right) + T_w \quad (15)$$

where $T_{A,m}$ is the antenna temperature [16], [17] being measured, T_w is the temperature of the radiometer waveguide, and V_r, V_h, and V_s are voltages of a square law detector, corresponding to the radiation sources of the two internal loads and the sky, respectively. All these voltages and temperatures on the right side of the equation are measured. The unknown parameter c is the parameter determined through the calibration and, as discussed in [14] and [18], c describes transmission losses due to a portion of waveguide and a microwave window in the system.

The ARM's system operates at 23.8 and 31.4 GHz. Other main system parameters are also listed in Table I. The system includes a noise diode injection device and an external blackbody reference target at an ambient temperature T_r. The radiometer equation of the system is given as [7]

$$T_{A,m} = \frac{T_{nd}}{V_{r+d} - V_r}(V_s - V_r) + T_r \quad (16)$$

where V_s is the voltage when the radiometer views the sky, V_{r+d} is the voltage when viewing the reference target with the noise diode on, V_r is the voltage when viewing the reference with the noise diode off, and T_{nd} is the noise injection temperature determined through the calibration. The radiation loss and emission of a microwave window in front of the radiometer antenna were measured in the laboratory and are assumed to be known and, because they are multiplicative with T_{nd}, are simply incorporated into it.

The radiometer (15) and (16) may be simplified for the sake of convenience to simulate the tipping data. We may write the parameters c in (15) as $r \cdot c_t$ and T_{nd} in (16) as $r \cdot T_{nd,t}$, where c_t and $T_{nd,t}$ are correct calibration factors, and r represents the correctness of the estimations of c or T_{nd}, with $r = 1$ representing a perfect calibration. With this consideration, (15) or (16) may be rewritten in the form as

$$T_{A,m} = r(T_A - T_g) + T_g \quad (17)$$

where $T_{A,m}$ is an estimate of the true antenna temperature T_A in the pointing direction, $T_g = T_w$ for the ETL's systems, and $T_g = T_r$ for ARM's system. We see that the measured antenna temperature is equal to true antenna temperature T_A when a calibration is performed without error ($r = 1$). We will refer to the factor r in (17) as the calibration factor. Equation (17) provides a convenient way to simulate the radiometric measurements in which the atmospheric antenna temperature T_A may be calculated using a radiative transfer and an antenna model. We will investigate the four frequency channels at 20.6, 22.235, 23.8, and 31.4 GHz, respectively. Although the frequency channel 22.235 GHz is not used in the ETL and ARM's systems, it is included here for reference.

III. TIPPING CALIBRATION METHOD

We first define the atmospheric airmass as the ratio of the opacity at the direction θ and the opacity at the zenith ($\theta = 90°$)

$$a(\theta) = \frac{\tau(\theta)}{\tau(90°)}. \quad (18)$$

In (18), for convenience, we have dropped the frequency dependence in notation. The tipping calibration method uses measurements of opacity, derived from measurements of T_b, as a function of airmass to derive a calibration factor. We will discuss later how T_b is derived from measurements of $T_{A,m}$. Equation (18) can be used to derive the calibration factor if the relationship between airmass a and the observation angle θ is known. In a plane-stratified atmosphere and if we ignore the bending of radiation rays caused by the gradient of refractive index, we have

$$a(\theta) = \frac{1}{\sin(\theta)}. \quad (19)$$

Sometimes, (19) is taken as the defining equation for airmass, but (18) is more general and includes (19) as a limiting case. Since (18) involves two opacities, the calibration procedure requires observations of at least two different angles θ_1 and θ_2. The measurements, $T_b(\theta_1, r)$ and $T_b(\theta_2, r)$ at the two angles are then mapped into τ_1 and τ_2 in opacity space by using (12) or (13). Note that we have explicitly expressed the measurements as a function of the calibration factor r. If we normalize τ_1 and τ_2 by their corresponding airmasses as $t_1 = \tau_1/a_1$ and $t_2 = \tau_2/a_2$, the normalized opacities t_1 and t_2 should theoretically have the same value, and any difference between them is due to an incorrect calibration factor. We may adjust r until an agreement between t_1 and t_2 is reached.

The calibration factor may also be derived equally well in the brightness temperature space. We may map the normalized opacities t_1 and t_2 back to zenith brightness temperatures, referred to as normalized brightness temperature T_{b1}^N and T_{b2}^N. They too should be equal to one another. Any difference between them can be adjusted with the calibration factor r. The concept of the normalized brightness temperature will be used in later analysis.

Authorized licensed use limited to: Susanne Crewell. Downloaded on March 29, 2009 at 09:05 from IEEE Xplore. Restrictions apply.

To reduce measurement uncertainties, tipping observations are often taken at more than two angles. Let $\{t_1, t_2, \cdots, t_n\}$ be the set of normalized opacities obtained from a set of observations. We may apply the least-square technique to obtain r by minimizing the sum of square differences between any pair of opacities $t_i(r)$ and $t_j(r)$, $(i = 1, n; j = 1, n)$

$$Q(r) = \frac{1}{2n^2} \sum_{i=1}^{i=n} \sum_{j=1}^{j=n} [t_i(r) - t_j(r)]^2 = \frac{1}{n} \sum_{i=1}^{i=n} [t_i(r) - \overline{t}(r)]^2 \tag{20}$$

where

$$\overline{t}(r) = \frac{1}{n} \sum_{i=1}^{i=n} t_i(r). \tag{21}$$

Minimization with respect to r yields the equation

$$F(r) = \sum_{i=1}^{i=n} (t_i - \overline{t})(z_i - \overline{z}) = 0 \tag{22}$$

where

$$z_i = \frac{1}{a(\theta_i)(T_{mr}(\theta_i) - T_b(\theta_i, r))} \frac{\partial T_b(\theta_i, r)}{\partial r},$$

and

$$\overline{z} = \frac{1}{n} \sum_{i=1}^{i=n} z_i. \tag{23}$$

Solving (22), we obtain the calibration factor r. Finding the zero of $F(r)$ is a well-posed mathematic problem as the curve of $F(r)$, shown in Fig. 1, suggests.

We can look at the calibration procedure in another way. Tipping data is a set of airmass-opacity pairs $\{(\tau_1, a_1), (\tau_2, a_2), \cdots, (\tau_n, a_n)\}$. The basic idea is that if we consider τ as a function of a, $\tau \equiv \tau(a)$, then $\tau(a = 0) = 0$ (i.e., τ extrapolated to airmass 0 is 0). Thus, these points of the pairs lie on a straight line that must pass the origin on the airmass-opacity plane, and the slope of the line is the zenith opacity. If the fitted line does not pass the origin, it implies an incorrect calibration factor. We may adjust the calibration factor r until the line passes the origin. The mathematical derivation is similar to the previous one. The difference is that the previous derivation minimizes the differences among the normalized opacities, while the line fitting method minimizes the differences between the opacities and a linear line that passes the origin. If only two angles are involved, the two methods are identical.

As pointed out by an anonymous reviewer, the metric of (20) could be replaced by a similar one involving the root-mean-square (rms) of the antenna temperature residuals. This metric would result in giving an rms residual that could be compared with the noise level of the radiometer. However, the present method could also give a similar rms residual after a mapping back from opacity space to antenna temperature space. Since the same basic information enters into both metrics, we don't think that the results would differ substantially.

There has been a less rigorous method that appears similar to the second method. Since it has been often used [15], [19]–[21], it is worth a brief discussion here. The method fits a line to a set of tipping data with an approximate calibration factor r. If the line's offset is not equal to zero, the line's slope is used as an approximation to the zenith opacity, which is then mapped into the zenith brightness temperature. Next, the zenith brightness temperature is used to obtain a new value of r from the radiometer equation. The process may be repeated until the offset of the line is near zero. The flaw of the method is that some of the information contained in the tipping data is lost in the process. For example, if the tipping observations are taken at angles with airmass 1, 2, and 3, the data at airmass 2 will never be used in the calibration process.

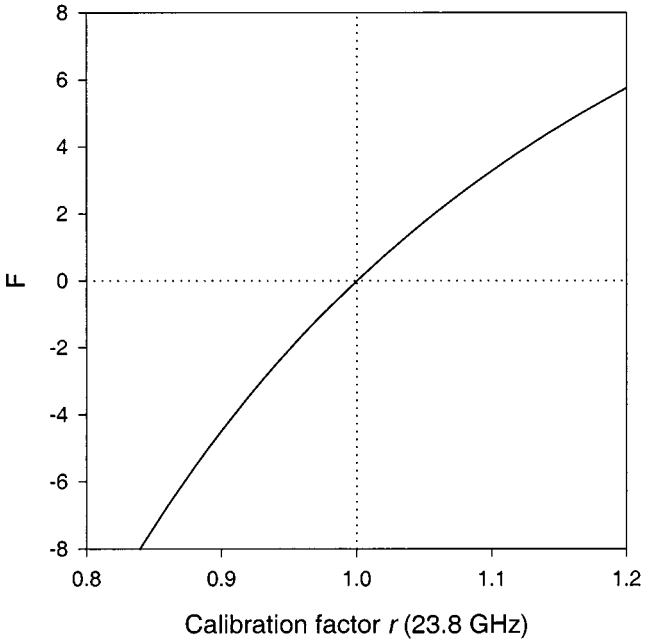

Fig. 1. Function given by (22), whose zero is the calibration factor.

IV. Calibration Errors and Methods to Reduce Them

Calibration errors may be caused by sources from the radiometer system and the violations of the assumptions in the theory on which the calibration is based. The former include the effect of radiometer antenna pattern, radiometer pointing error and system random noise. The latter include the uncertainty in the mean radiating temperature and the uncertainties in the fundamental relationship (19) between the airmass and the observation angles, which can be affected by nonstratified atmospheric conditions and the earth's curvature.

We simulated these error sources and developed and tested effective techniques to reduce them. The simulations were performed by using a radiative transfer model [22] and the simplified radiometer (17) for a clear-sky atmosphere, which is represented by radiosonde pressure, temperature, and humidity profiles. A statistical ensemble of radiosonde data, referred to as S with a size of 16 380 soundings, was collected from five stations around the area of Oklahoma City, OK, from 1966 to 1992.

To evaluate a calibration, we first need to define the calibration error. Although the quantity $\Delta r = r - 1$ (the difference between the calibration factor r and its correct value $r = 1$), can be used as a measure to the error, it may be more intuitive to express the error in terms of the brightness temperature. How-

Authorized licensed use limited to: Susanne Crewell. Downloaded on March 29, 2009 at 09:05 from IEEE Xplore. Restrictions apply.

TABLE II
COLUMNS A: rms DIFFERENCES BETWEEN TWO MODEL CALCULATIONS OF T_b, ONE WITH REFRACTIVE INDEX CONSIDERED AND THE OTHER WITHOUT; COLUMNS B: rms DIFFERENCES BETWEEN TWO MODEL CALCULATIONS, ONE WITH EARTH CURVATURE CONSIDERED AND THE OTHER WITHOUT. THE DIFFERENCES (K) ARE LISTED AS A FUNCTION OF FREQUENCY (GHz) (ROW 1) AND AIRMASS (COLUMN 1)

Freq.→ Airmass ↓	20.6 (A)	22.235 (A)	23.8 (A)	31.4 (A)	20.6 (B)	22.235 (B)	23.8 (B)	31.4 (B)
1.5	0.00	0.00	0.00	0.00	0.02	0.02	0.02	0.01
2	0.01	0.01	0.01	0.01	0.05	0.07	0.06	0.04
3	0.03	0.04	0.04	0.02	0.16	0.23	0.19	0.13
4	0.07	0.09	0.08	0.06	0.35	0.48	0.40	0.30

ever, for a given error Δr, the error in corresponding antenna temperature depends on the magnitude of the temperature itself. For simplicity, we evaluate the error at a reference temperature $\langle T_b \rangle$. That is, for a calibration with an error Δr, the calibration error is defined using (17) as

$$\mathrm{err}_{\mathrm{cal}} = \Delta r(\langle T_b \rangle - T_g). \tag{24}$$

We use the climatological mean of the brightness temperature as the reference temperature. The values of the reference temperatures are 27.2, 40.0, 35.0, and 18.5 K for the four selected channels at 20.6, 22.235, 23.8, and 31.4 GHz, respectively.

Theoretically, any set of angles with two or more being distinct can be included in the tipping observations. However, because of the various uncertainties, at least two of the angles (or their corresponding airmasses) should not be too close. In addition, low elevation angles or large airmasses should also be avoided due to the finite beam width. Our data simulations include five elevation angles at 90°, 41.8°, 30°, 19.5°, and 14.5°, corresponding to airmasses 1, 1.5, 2, 3, and 4. To reveal the angular dependence of the tipping calibration, we perform calibrations using tipping data at two elevation angles, with one fixed at zenith and the other varying among the remaining angles. Thus, from a set of tipping data taken at the five angles, we may have four values of the calibration factor for a single radiometer channel.

A. Effect of Earth Curvature and Atmospheric Refractive Index

As we discussed earlier, (19) is for a plane horizontally stratified atmosphere with a refractive index profile independent of height. For the earth's atmosphere, however, the earth curvature and the vertical gradient of the refractive index cause the amount of airmass at an elevation angle to differ from that given by (19) [22]. Under normal conditions, the vertical gradient of the refractive index "bends" a radiation ray downward and thus results in a larger airmass than if there were no such gradient. We computed T_b using a computer code [22] that uses ray tracing methods based on Snell's Law for a spherical atmosphere and ran the code twice for each profile in our statistical ensemble: once with the refractive index n calculated from a radiosonde profile and the second time with n set to unity. As shown in the A Columns in Table II, the rms differences between the two with and without considerations of the gradient are very small at all of the selected airmasses, about a few hundredths of a degree. Thus, the effect of the refractive index profile on system calibration is negligible. Table II is computed from the statistical ensemble S.

Earth curvature has a relatively large effect, which causes airmass at an angle θ to be smaller than that of an atmosphere with a flat surface at the same angle. The differences between the two brightness temperatures with and without the earth curvature are about one or two tenths of a degree at airmass 3 and three- to five-tenths of a degree at airmass 4 (see the B Columns in Table II). Although the effect is still small when compared to those from other sources, the airmass can be conveniently corrected to a large degree. In a spherically stratified atmosphere and neglecting the gradient of refractive index, the atmospheric opacity τ is given by

$$\tau(\theta) = \int_0^\infty \frac{\alpha\, dz}{\sqrt{1-(\cos\theta/(1+z/r_e))^2}} \tag{25}$$

where θ is the radiometer elevation angle, r_e (=6370.95 km) is the earth's radius, and α is the absorption coefficient. Since the absorption coefficient α decreases with height z almost exponentially with a scale height of 2–3 km [23], the value of the ratio (z/r_e) is a small quantity in the range where the absorption has a contribution to the integrand. Thus, we may expand the denominator in (25) with respect to (z/r_e) and derive an approximation as

$$\tau(\theta) = \frac{\tau(90°)}{\sin\theta} - \frac{1}{r_e\sin(\theta)}\left(\frac{1}{\sin^2(\theta)}-1\right)\int_0^\infty \alpha z\, dz \tag{26}$$

where $\tau(90°)$ is the zenith opacity. If we define an effective height H such that

$$H = \frac{1}{\tau(90°)}\int_0^\infty \alpha z\, dz$$

then the integral in the above equation may be written as a multiple of the zenith opacity $\tau(90°)$ and H. We note that if the absorption decays exponentially, then the effective height is equal to the absorption scale height. Thus, we have

$$\tau(\theta) = \left[\frac{1}{\sin\theta} - \frac{H}{r_e\sin(\theta)}\left(\frac{1}{\sin^2(\theta)}-1\right)\right]\tau(90°). \tag{27}$$

According to its definition (18), the airmass in a spherical atmosphere is

$$a = a_0 - Ha_0(a_0^2-1)/r_e \tag{28}$$

where a_0 is airmass in a plane stratified atmosphere, given by (19). As an example, we derived the average effective height

Authorized licensed use limited to: Susanne Crewell. Downloaded on March 29, 2009 at 09:05 from IEEE Xplore. Restrictions apply.

TABLE III
H–EFFECTIVE HEIGHT (km) AND ITS STANDARD DEVIATION (km)

20.6 GHz		22.235 GHz		23.8 GHz		31.4 GHz	
H	STD	H	STD	H	STD	H	STD
1.9	0.3	2.1	0.4	1.9	0.4	2.3	0.4

H and its standard deviation from a subset of the statistical ensemble S, which is about a half of the size of S. The subset is referred to as set S_1. The effective height is computed using (27), where the opacity is calculated from the model in which both the earth curvature and refractive index are included. Thus, the obtained effective height H contains the effect of refractive index profile, and its value is slightly less than one that does not consider the effect of refractive index, due to the reasons discussed earlier. Table III lists the effective height for the four frequency channels.

The use of the airmass-angle relationship (19) without a correction causes calibration errors, resulting in measurements with values lower than their true values as shown in A Columns in Table IV. The error increases with the increase of airmass. After the airmass corrections using (28), the errors are reduced about a factor of 5 (see Table IV). Results of Table IV are obtained from a test data set, referred to as S_2, a subset half of the size of S, independent of S_1.

B. Effect of Antenna Beam Width

The antenna temperature $T_A(\theta, \varphi)$ of a radiometer at a specified frequency and direction θ, φ is a weighted average of incoming brightness temperature $T_b(\eta', \xi')$ over all directions η', ξ' [18]

$$T_A(\theta, \varphi) = \frac{\int_0^{2\pi}\int_0^{\pi} P(\theta, \varphi; \eta', \xi') T_b(\eta', \xi') \sin(\eta')\, d\eta'\, d\xi'}{\int_0^{2\pi}\int_0^{\pi} P(\theta, \varphi; \eta', \xi') \sin(\eta')\, d\eta'\, d\xi'}. \quad (29)$$

In (29), $P(\theta, \phi; \eta', \xi')$ is the power pattern of the radiometers antenna. Under normal atmospheric conditions and at the weakly absorbing frequencies considered here, due to the nonlinear increase of the brightness temperature when lowering the elevation angle, T_A is larger than that of the brightness temperature T_b^c at a cone-like antenna beam center direction. Fig. 2 shows their difference $T_A - T_b^c$ as a function of the antenna beam width (3-dB beam width of an antenna with a corrugated feed horn) for a 23.8 GHz radiometer under a typical sky condition with PWV $= 3.2$ cm at three elevation angles. The antenna power pattern in the calculation is for a corrugated feed horn [24]. We see that the difference increases with the increase of the beam width. For a 5.7° antenna beam width, the difference is 0.47, 1.05, or 1.72 K at the angle with an airmass of 2, 3, or 4, respectively. The difference also depends on the amount of atmospheric water vapor. Fig. 3 shows the difference (filled symbols) as a function of PWV for about 4000 selected samples in the ensemble S. The concave-down features shown in the figure reflect that the magnitude of the nonlinear variation of the brightness temperature across the antenna beam varies with the amount of PWV. At large airmass (or low elevation angle), the magnitude may reach a peak, as the figure shows.

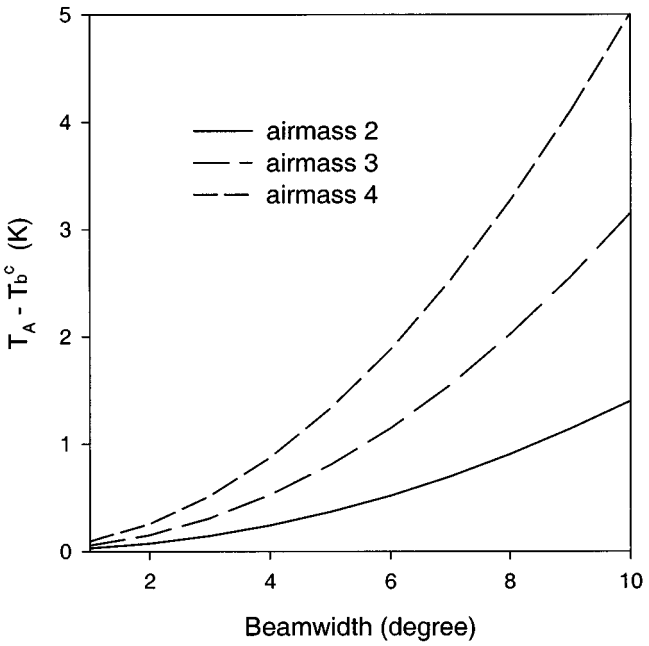

Fig. 2. Differences between antenna temperature and the brightness temperature at the beam center direction as a function of antenna beam width. The antenna gain pattern is modeled for a corrugated feed horn. The three curves correspond to the differences when the antenna views a clear sky with PWV $= 3.2$ cm at airmass 2, 3, or 4, respectively.

Due to the finite antenna beam width, the airmass-angle relationship is no longer correctly given by (28), which is applicable for a radiometer with an infinitely small beam width. Calibrations using (28) for a radiometer with a finite antenna beam width are accompanied by errors, as shown in the A Columns in Table V(a) for a 4° beam width and Table V(b) for a 5.7° beam width. The errors from a 5.7° beam width are about twice as large as those for a 4° beam width. Another significance in the table is the increase of the errors with the increase of airmass. For example, for the same beam width, the calibration errors at airmass 3 is about 50% more than those at airmass 2. For a 23.8 GHz radiometer with a 5.7° antenna beam width, the calibration error is about $+0.5$ K when airmass 3 is used along with airmass 1. The significance of these errors calls for a correction for the airmass given by (28) or, equivalently, an adjustment of the measured antenna temperature to that at the antenna beam center. We adopt the latter to adjust T_A to T_b^c. After the adjustment, (28) can then be applied. The amount of adjustment δT_A is derived (see Appendix) by assuming a Gaussian beam and is given as

$$\delta T_A(\theta) = \frac{\theta_{1/2}^2}{16\,\mathrm{Ln}(2)} (T_{mr}(\theta) - T_{bb}) \cdot \exp(-\tau(\theta))[2 + (2 - \tau(\theta))\tan^{-2}(\theta)]\tau(\theta) \quad (30)$$

where $\theta_{1/2}$ is in radians and is the full width at half-maximum power of the power pattern. Note that the τ in (30) is the slant path opacity at an elevation angle θ. The observed antenna temperatures should be corrected by the amount given by (30) before being used in the calibrations: $T_b^c = T_A - \delta T_A$. Note that

Authorized licensed use limited to: Susanne Crewell. Downloaded on March 29, 2009 at 09:05 from IEEE Xplore. Restrictions apply.

TABLE IV
Rms CALIBRATION ERRORS BEFORE (A) AND AFTER (B) AIRMASS CORRECTIONS, IN WHICH THE SCALE HEIGHTS IN TABLE III ARE USED. THE ERRORS (K) ARE LISTED AS A FUNCTION OF FREQUENCY (GHz) (ROW 1) AND AIRMASS PAIR (COLUMN 1) AT WHICH THE TIPPING-CURVE DATA ARE SIMULATED AND USED IN THE CALIBRATIONS

Freq.→ Airmass pair ↓	20.6 (A)	20.6 (B)	22.235 (A)	22.235 (B)	23.8 (A)	23.8 (B)	31.8 (A)	31.8 (B)
1, 1.5	0.05	0.02	0.07	0.03	0.06	0.03	0.07	0.05
1, 2	0.06	0.02	0.10	0.03	0.09	0.03	0.08	0.05
1, 3	0.11	0.02	0.18	0.03	0.14	0.03	0.12	0.05
1, 4	0.17	0.03	0.28	0.04	0.21	0.04	0.16	0.05

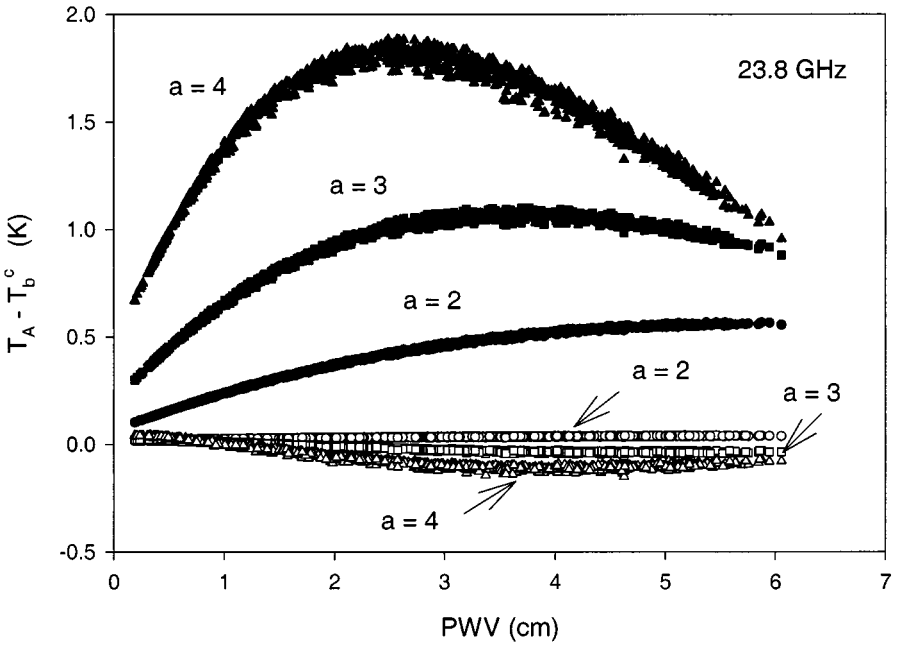

Fig. 3. Differences between antenna temperature and the brightness temperature at the beam center direction as a function of PWV. The filled symbols are those without beam effect corrections. The open symbols are those with the corrections, in which the antenna temperature is adjusted by an amount given by (30). The airmasses at which the differences are calculated are indicated in the figure. Data used in the simulations are explained in the text.

the amount of brightness temperature adjustment is itself a function of the brightness temperature, whose correct value is unknown before the calibration. In practice, we may derive δT_A by an iteration process. First, the calibration is carried out without the adjustment. Then, the calibration is repeated but with an adjustment. Two steps are usually sufficient for the calibration. The open symbols in Fig. 3 represent the differences between the adjusted calculated antenna temperature $(T_A - \delta T_A)$ and the brightness temperature at the beam center T_b^c. The differences are reduced by one order of magnitude over those without such adjustment (filled symbols).

The corrections of antenna beam effect using (30) significantly reduces the calibration errors as shown in B columns in Table V. However, the effect of antenna beam width is a complicated issue. In reality, the beam's side lobes may pick up radiation at low elevation angles from sources that are unpredictable. For example, radiation from the ground that enters the antenna sidelobes is a contaminating factor. For this reason and some others discussed later, tipping observations should avoid low elevation angles. Our experiences suggest that angles with airmasses larger than 3 should be avoided, especially for the 6° antenna used by ARM.

C. Errors Caused by Uncertainties in Radiometer Pointing Angle

In a Cartesian XYZ coordinate system where a radiometer is located at the origin, we define zenith as the z direction and let the YZ plane contain the antenna beam center. The pointing angle or elevation angle θ is then defined as the angle between the positive Y axis and the beam center direction. For a radiometer that is able to point any direction in the YZ plane, we refer to a pair of *symmetric angles* as a pointing angle θ and its reflection in the XZ plane, the angle $180° - \theta$. We may also refer the *one side* or *two sides* as the one or two of the half spaces in the YZ plane separated by the Z axis (zenith vector). Radiometer systems often use reflectors to direct radiation to the

Authorized licensed use limited to: Susanne Crewell. Downloaded on March 29, 2009 at 09:05 from IEEE Xplore. Restrictions apply.

TABLE V
rms CALIBRATION ERRORS BEFORE (A) AND AFTER (B) ANTENNA BEAM WIDTH CORRECTIONS. (a) FOR A 4° BEAM WIDTH ANTENNA AND (b) FOR A 5.7° BEAM WIDTH ANTENNA. THE ERRORS (K) ARE LISTED AS A FUNCTION OF FREQUENCY (GHz) (ROW 1) AND AIRMASS PAIR (COLUMN 1), AT WHICH THE TIPPING CURVE DATA ARE SIMULATED AND USED IN CALIBRATIONS

(a)

Freq.→ Airmass pair ↓	20.6 (A)	20.6 (B)	22.235 (A)	22.235 (B)	23.8 (A)	23.8 (B)	31.8 (A)	31.8 (B)
1, 1.5	0.11	0.01	0.16	0.01	0.13	0.01	0.04	0.03
1, 2	0.15	0.01	0.21	0.01	0.18	0.01	0.06	0.04
1, 3	0.25	0.03	0.30	0.03	0.28	0.04	0.14	0.05
1, 4	0.37	0.03	0.40	0.04	0.40	0.04	0.24	0.05

(b)

Freq.→ Airmass pair ↓	20.6 (A)	20.6 (B)	22.235 (A)	22.235 (B)	23.8 (A)	23.8 (B)	31.8 (A)	31.8 (B)
1, 1.5	0.20	0.01	0.28	0.02	0.24	0.02	0.10	0.03
1, 2	0.29	0.02	0.39	0.04	0.34	0.04	0.16	0.05
1, 3	0.49	0.06	0.59	0.09	0.56	0.08	0.31	0.07
1, 4	0.74	0.08	0.77	0.10	0.79	0.10	0.52	0.07

TABLE VI
Rms CALIBRATION ERRORS CAUSED BY A 1° SHIFT OF THE ELEVATION ANGLES AS A FUNCTION OF THE FREQUENCIES (GHz) (ROW 1) AND AIRMASS PAIR (COLUMN 1). (a) CALIBRATIONS IN WHICH TIPPING DATA ARE TAKEN AT ONE SIDE ONLY AND (b) CALIBRATIONS IN WHICH DATA FROM BOTH SIDES ARE USED

Freq.→ Airmass pair ↓	20.6 (A)	22.235 (A)	23.8 (A)	31.65 (A)	20.6 (B)	22.235 (B)	23.8 (B)	31.65 (B)
1, 1.5	1.63	2.61	2.14	1.01	0.03	0.05	0.04	0.02
1, 2	1.70	2.72	2.24	1.05	0.05	0.07	0.06	0.03
1, 3	2.12	3.39	2.78	1.30	0.10	0.15	0.13	0.06
1, 4	2.61	4.19	3.43	1.61	0.16	0.25	0.21	0.10

antenna. The slant path measurements are accomplished by rotating the reflectors. The reflector rotating angles, the alignment between the antenna and the reflector, and the positioning of the total system all affect the pointing (elevation) angles.

To see the impact of the pointing error on the calibration, we use data in S to simulate the calibrations in which all the observation angles in the plane of scanning are off by 1°. As shown in A Columns in Table VI, the pointing errors could have serious impact on the performance of the tipping calibration if only one-side tipping calibration is used. Also shown in the table is that the same pointing errors cause larger calibration uncertainties when data with larger airmasses (lower elevation angles) are used than those with small airmasses (higher elevation angles). The pointing angle errors can often be identified by performing tipping observations at symmetric angles. If the measurements at an angle consistently differ from those at its symmetric angle, it usually implies the existence of the pointing error (except in the situations when there is a persistent horizontal inhomogeneity in the atmosphere). However, if one were to perform tipping calibrations on a moving platform, the diagnosis of angular errors would be much more complex.

Fortunately, the effect of the pointing error can often be reduced significantly by using tipping data taken on both sides under the condition that the differences among those angles are known precisely. This is due to the effect that the uncertainties in the measurements on one side due to the pointing error are partially canceled out by the uncertainties of those on the other side. As shown in the B Columns in Table VI, the calibration

Authorized licensed use limited to: Susanne Crewell. Downloaded on March 29, 2009 at 09:05 from IEEE Xplore. Restrictions apply.

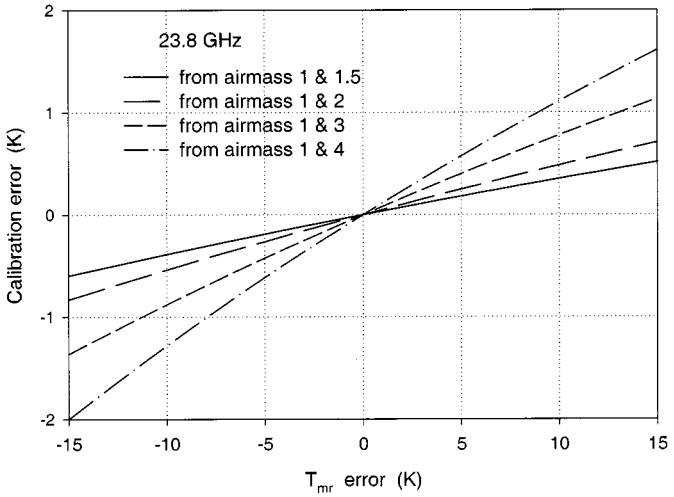

Fig. 4. Calibration errors at 23.8 GHz channel as a function of errors of the mean radiating temperatures. The calibration errors also show dependence on the observation airmasses (or angles), at which data are taken and used in the calibrations. The atmospheric state for this example has a zenith brightness temperature of 59.2 K.

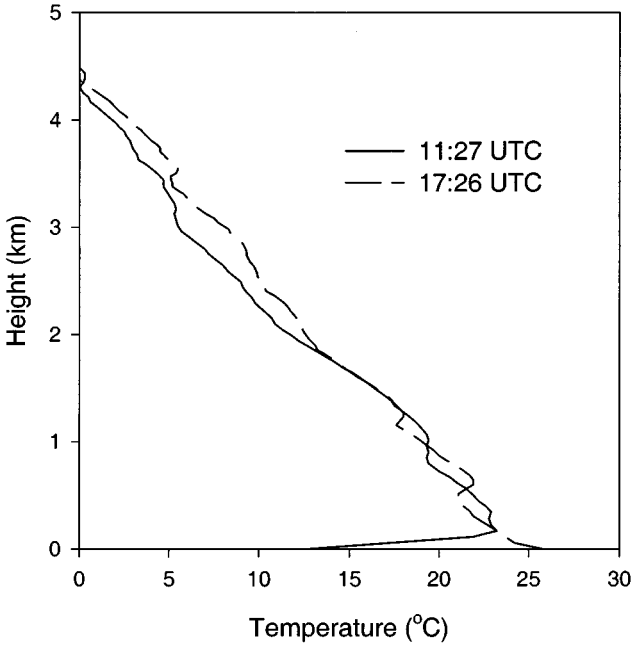

Fig. 5. Nocturnal temperature profile showing temperature inversion (solid line) and a daytime profile with normal lapse rate (dashed line).

errors are reduced to a negligible level after we use tipping data from both sides. This strongly suggests that tipping data should be taken in pairs on the symmetric elevation angles.

D. Effect of Mean Radiating Temperature

The mean radiating temperature T_{mr} plays a role in mapping the brightness temperature T_b to the opacity τ. Traditionally, T_{mr} is treated as a constant and is determined climatologically. For zenith observations, the uncertainties T_{mr} are usually not a crucial factor [10], because the brightness temperatures are usually small, resulting in small uncertainties in opacity, as seen from the mapping function (12) or (13). But in tipping observations, the brightness temperature can be large at a low elevation angle. Fig. 4 shows an example of how the T_{mr} uncertainties (which are generated by adding the same error to both T_{mr} at the two airmasses) affect the calibrations. As listed in Table VII(a), the climatological variations of T_{mr} are about 9 K, estimated using data in S_1. Thus, we see from Fig. 4 that the uncertainties in T_{mr} may cause significant calibration errors when large airmasses are used. The T_{mr} uncertainties can be reduced by dividing the T_{mr} climatology into seasons, a method that has been practiced at ETL for many years.

Another method that reduces the uncertainties significantly is the predicting T_{mr} from the surface air temperature T_s, using regression analysis. Surface-based temperature measurements along with calculated T_{mr} using radiosonde measurements are used to derive linear regression coefficients relating surface temperature to T_{mr}. Table VII(b) lists the linear regression coefficients for prediction of T_{mr} and the standard error of estimation (SEE) after the regression. To simulate the effect of errors in the measurement of T_s, a 0.5 K Gaussian random noise ε is added to the radiosonde value, and $T_s + \varepsilon$ is used as a predictor. As shown in the table, the T_{mr} uncertainties are cut in half by using the T_s measurements. However, the T_{mr} prediction from T_s is often poor when strong temperature inversions occur. In Fig. 5, the solid curve represents a nocturnal temperature inversion, while the dashed curve is a daytime profile with normal lapse rate. Using the regression coefficients in Table VII(b) and the surface temperatures of the two profiles in Fig. 5, the prediction yields a T_{mr} for the daytime profile differing by about 1.6 K from the true value and that for the nocturnal profile differing by about 7.9 K. The prediction can be improved significantly by using boundary temperature profiles from a 60 GHz radiometric temperature profiler [25], which accurately recovers boundary layer surface temperature inversions or a radio acoustic sounding system [26].

To see the effects of the T_{mr} uncertainties, we applied T_{mr} separately from Table VII to the calibrations using data from S_2. The results are summarized in the A columns for the uses of climatological mean and B Columns for the uses of surface temperature in Table VIII, which strongly suggests that the use of surface temperature can significantly improve the calibration accuracy.

E. Errors Caused by System Random Noise

The system random noise also affects calibration accuracy. To estimate its influence on system absolute accuracy, we performed tipping calibrations using simulated tipping data from S with a 0.1 K Gaussian white noise. The results are shown in Table IX. The calibration uncertainties are about 0.1° to 0.4°. Also shown in the table is that the uses of larger airmass differences suffer less than the uses of smaller airmass differences. The impact of the system noise can always be reduced by time averaging of a time series of calibration factors.

F. Errors Caused by Uncertainty in the Offset of the Radiometer Equation

In the analysis so far, we have assumed that the offset of the radiometer equation is known precisely. In reality, however, uncertainty may exist. To estimate the impact of the uncertainty on

Authorized licensed use limited to: Susanne Crewell. Downloaded on March 29, 2009 at 09:05 from IEEE Xplore. Restrictions apply.

TABLE VII
(a) THE CLIMATOLOGICAL MEANS OF THE MEAN RADIATING TEMPERATURES (K) AND THEIR STANDARD DEVIATIONS (K) AT THE FREQUENCIES (GHz) AND AIRMASSES LISTED IN ROW 1 AND COLUMN 1, RESPECTIVELY. (b) THE LINEAR REGRESSION COEFFICIENTS c_0 AND c_1 USED FOR PREDICTION OF THE MEAN RADIATING TEMPERATURES AND STANDARD ERRORS OF ESTIMATION (SEE) AFTER THE REGRESSION AT THE FREQUENCIES (GHz) AND AIRMASSES LISTED IN ROW 1 AND COLUMN 1, RESPECTIVELY

Freq.→ Airmass ↓	T_{mr} 20.6	STD 20.6	T_{mr} 22.235	STD 22.235	T_{mr} 23.8	STD 23.8	T_{mr} 31.65	STD 31.65
1	277.7	8.8	277.0	8.5	278.0	8.8	274.5	9.4
1.5	277.9	8.8	277.3	8.6	278.2	8.9	274.6	9.4
2	278.0	8.9	277.5	8.7	278.4	8.9	274.8	9.4
3	278.3	9.0	278.1	8.9	278.8	9.1	275.0	9.5
4	278.6	9.2	278.6	9.2	279.2	9.3	275.3	9.6

(a)

	c_0, c_1 20.6	SEE 20.6	c_0, c_1 22.235	SEE 22.235	c_0, c_1 23.8	SEE 23.8	c_0, c_1 31.65	SEE 31.65
1	266.5 0.721	3.8	266.3 0.690	3.7	266.8 0.720	3.8	262.6 0.765	4.2
1.5	266.6 0.732	3.8	266.4 0.701	3.7	266.9 0.728	3.8	262.7 0.768	4.2
2	266.6 0.732	3.8	266.5 0.712	3.8	267.0 0.735	3.8	262.8 0.771	4.2
3	266.8 0.743	3.8	266.7 0.733	3.8	267.1 0.751	3.8	263.0 0.777	4.2
4	266.9 0.754	3.9	266.9 0.752	3.9	267.3 0.765	3.9	263.2 0.783	4.2

(b)

TABLE VIII
RMS CALIBRATION ERRORS USING T_{mr} GIVEN BY CLIMATOLOGICAL MEANS (COLUMNS A) AND PREDICTED FROM SURFACE AIR TEMPERATURES (COLUMNS B), AS A FUNCTION OF FREQUENCY (GHz) AND AIRMASS PAIR

Freq.→ Airmass pair ↓	20.6 (A)	20.6 (B)	22.235 (A)	22.235 (B)	23.8 (A)	23.8 (B)	31.4 (A)	31.4 (B)
1, 1.5	0.12	0.04	0.38	0.13	0.23	0.07	0.04	0.02
1, 2	0.17	0.06	0.53	0.18	0.33	0.10	0.06	0.02
1, 3	0.27	0.09	0.91	0.30	0.54	0.18	0.09	0.03
1, 4	0.39	0.12	1.41	0.45	0.80	0.26	0.12	0.04

the system calibration, we shifted the system offset by adding $\Delta Off = 1$ K to the right side of the radiometer (17) and then used it to simulate tipping measurements. It would seem that a positive one-degree offset shift would cause a positive one-degree measurement error. In fact, the tipping calibration compensates for the positive shift by adjusting the calibration factor r upward (becoming large than 1) with an amount of Δr (a value about 0.003). Thus from (17), the measurement error is given by $\Delta r(T_A - T_g) + \Delta Off (< \Delta Off)$. The calibration errors (at our reference brightness temperatures) are about 0.1 K for all the four channels considered here. However, it is easy to see that the measurement error increases with the sky brightness temperature being measured. At $T_A = 100$ K, the calibration errors are about 0.3 K. Thus, as long as the offset uncertainty is controlled under 1 K, it will not cause serious calibration problems. However, as pointed out by an anonymous reviewer, these conclusions are valid only if frequent tipping calibrations are available. If there are hours or days between such calibration, then changes in offset will not be compensated between these periods.

Authorized licensed use limited to: Susanne Crewell. Downloaded on March 29, 2009 at 09:05 from IEEE Xplore. Restrictions apply.

TABLE IX
Rms CALIBRATION ERRORS (K) IN WHICH THE SIMULATED TIPPING DATA ARE CONTAMINATED WITH 0.1 K GAUSSIAN RANDOM NOISE

Freq (GHz).→ Airmass pair ↓	20.6	22.235	23.8	31.65
1, 1.5	0.37	0.38	0.37	0.37
1, 2	0.23	0.24	0.23	0.22
1, 3	0.16	0.17	0.17	0.16
1, 4	0.14	0.15	0.15	0.14

G. Errors Caused by Nonstratified Atmospheric Conditions

The airmass-angle relationship (28) requires a horizontally stratified atmosphere. This is the reason why calibrations are usually performed under clear-sky conditions. However, even under these conditions, caution must be exercised due to spatial variations of the water vapor and temperature fields. An example of horizontal inhomogeneity is shown Fig. 6. In the figure, the three curves are time series of radiometric measurements taken by the ARM's MWR during WVIOP'97. The dotted curve is taken at zenith direction, and the other two curves (brightness temperatures normalized to zenith) are taken at 30° and 150° (airmass 2). We see significant differences and even phase shifts between these curves. To estimate the effect of horizontal inhomogeneity and to evaluate methods to reduce its impact, we simulated horizontal inhomogeneity in the tipping data. Data available for such simulations are from water vapor Raman lidars during the WVIOP97 and a similar experiment in 1996 (WVIOP'96). Data of pressure and temperature fields with horizontal inhomogeneity are not available. Fortunately, the effects of the horizontal variations in the two fields are secondary compared with that of water vapor. Air pressure and temperature are obtained from balloon soundings from the BBSS that were released every 3 h during the two experiments.

There have been many studies and reports that Raman lidars can provide vertical soundings of water vapor mixing ratio that are comparable in accuracy to radiosonde measurements [27]. However, Raman lidars are limited by clouds that rapidly attenuate the laser beam and background skylight during daytime. Therefore, only nighttime and clear-sky data are used in the simulations. In our first set of simulations, the water vapor fields are obtained from the NASA/Goddard Space Flight Center water vapor Raman lidar [28] during WVIOP'96. The lidar has a range covering from 0.15 to 8.0 km with a range resolution of 75 m. One of the lidar operation modes during the experiment was slant path observations at elevation angles 90°, 20°, 10°, and 5°. Since the low elevation angles are usually avoided in the tipping observations, we simulated tipping data at 90° and 20° directions only. The data available to us were five one-hour time series, taken on five different days. The time series have 12-min temporal resolution; i.e., the measurements at the five angles are repeated every 12 min. The near surface water vapor is not measured by the lidar. It is obtained from the surface meteorological observation system (SMOS), collocated with the lidar. The water vapor field beyond the maximum range is obtained from the latest released balloon soundings from BBSS and is assumed horizontally homogeneous. The pressure and temperature fields along the slant paths are also obtained from the balloon soundings and are assumed horizontally homogeneous.

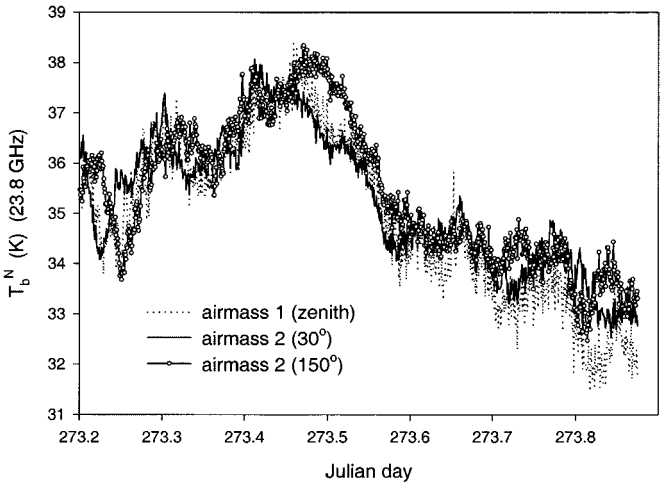

Fig. 6. Normalized brightness temperature measurements taken during WVIOP'97. The three curves correspond to brightness temperatures observed at airmass 1 and a pair of symmetric elevation angles with airmass 2. The figure demonstrates the horizontal inhomogeneity even under clear-sky conditions, in contrast to a stratified atmosphere, which should result in an agreement among the three curves.

TABLE X
RMS CALIBRATION ERRORS (K) OF TIPPING CALIBRATIONS IN WHICH A PAIR OF SIMULATED TIPPING DATA AT ZENITH AND 20° ELEVATION ANGLE ARE USED. THE TIPPING DATA ARE SIMULATED USING DATA MEASURED BY THE NASA/GSFC's RAMAN LIDAR. EACH VALUE LISTED HAS A SAMPLE SIZE OF 8

	20.6	22.235	23.8	31.65
Sep. 20	0.36	0.56	0.47	0.17
Sep. 21	0.71	1.12	0.94	0.33
Sep. 28	0.31	0.51	0.41	0.13
Sep. 29	0.82	1.27	1.08	0.40
Sep. 30	0.18	0.32	0.23	0.08

The effect of water vapor fields beyond the lidar maximum range will not significantly reduce the representativeness of the simulated brightness temperatures. At the zenith direction, the lidar reaches a height of 8 km. The contributions to the radiometer received power from water vapor above that level is negligible. At the 20° observation angle, the lidar reaches a height of 2.7 km at a horizontal distance of 7.5 km. In the middle-latitudes, about 75% of water vapor is contained in the air between the surface and the 2.7 km level. In addition, due to the surfaceair interaction, water vapor in the boundary layer varies much more than that above the boundary layer.

From the above data fields, we simulated one-sided tipping data at the two lidar observation angles corresponding to airmasses 1 and 3, respectively. No system noise was added in the simulations to isolate the effect of the inhomogeneity. Table X shows statistics of the calibration accuracy (without time averaging). We see that the accuracies vary over different days. The calibrations on September 21 and 29 would usually not be acceptable.

Authorized licensed use limited to: Susanne Crewell. Downloaded on March 29, 2009 at 09:05 from IEEE Xplore. Restrictions apply.

TABLE XI
RMS CALIBRATION ERRORS (K) AS A FUNCTION OF FREQUENCY (GHz) (ROW 1) AND AIRMASS PAIR (COLUMN 1). COLUMN A: TIPPING DATA ON ONE SIDE ARE USED, COLUMN B: TIPPING DATA ON BOTH SIDES ARE USED. SAMPLE SIZE = 1296

Freq (GHz).→ Airmass pair ↓	20.6 (A)	20.6 (B)	22.235 (A)	22.235 (B)	23.8 (A)	23.8 (B)	31.4 (A)	31.4 (B)
1, 1.5	0.80	0.54	1.31	0.88	1.07	0.72	0.38	0.26
1, 2	0.70	0.45	1.14	0.74	0.93	0.60	0.33	0.23
1, 3	0.70	0.43	1.16	0.72	0.94	0.60	0.32	0.20
1, 4	0.77	0.47	1.28	0.81	1.04	0.64	0.35	0.21

Although the data from the NASA/GSFC Raman lidar enable us to simulate radiometric measurements using data directly along the slant path, the data set is limited by short duration and by the fact that the data were taken only on one side. It will be shown later that time averaging and taking tipping ovservations on both sides are important techniques to improve calibration. For this reason, we simulated a second set of tipping curves from data taken by the ARM's Raman lidar during WVIOP'97 [29]. Because the lidar was operated in zenith mode during the experiment, conversion of time series to spatial series is needed. The conversion is accomplished by using wind data from BBSS during the experiment. The ARM lidar has a temporal resolution of 2 min and a height coverage from 0.136 km to about 8 km with a range resolution of 78 m. We selected five nighttime clear sky periods, each about 12 h. We converted the time series of the profiles into a series of height-distance cross sections with two minute intervals. Let $F = \{\boldsymbol{f}_i, i = 1, \cdots, n\}$ be the profile time series with a constant time interval δt between any two adjacent profiles. Extract m consecutive profiles $F_i = \{\boldsymbol{f}_{i+k}, k = 0, \cdots, m(m < n-1)\}$ from F. The horizontal distance $x_{m-k,j}$ of a data point $P_{i+k}(z_j)$ of the profile $\boldsymbol{f}_{i+k}$ at a time t_{i+k} at a height z_j is given by

$$x_{0,j} = 0, \qquad x_{m-k,j} = \sum_{q=1}^{m-k} u_{i+m-q,j}\delta t (k = 0, \cdots, m-1) \tag{31}$$

where $u_{i,j}$ is the mean horizontal wind at a height z_j between the times t_{i-1} and t_i, at which two consecutive profiles are taken. The horizontal dimension L_x of the height-distance cross section is set to be over 22 km (i.e., all time-advected height levels extended at least to 22 km) to ensure that at an elevation angle of about 20°, the radiometer observes at least 85 water vapor within this cross section. The radiometer is located at the ground $z = 0$ and $L_x/2$ km from the point $x = 0$, so that tipping data can be simulated on both sides in 0, $L_x/2$ and $L_x/2, L_x$. The near surface water vapor, not provided by the lidar, is obtained from the SMOS. The pressure and temperature profiles were obtained from the 3 h interval balloon soundings from BBSS by interpolations of the data points into the lidar time-height profile grids. Data beyond the boundary $x = 0$ and $x = L_x$ are assumed to have the same values as those at the boundary. The water vapor field above the Raman profiles are also obtained from the balloon soundings.

From the above data fields, we simulated tipping data time series. Each data unit consists of five data pairs: two measurements at a pair of symmetric angles at each of the airmasses 1, 1.5, 2, 3, and 4. In the A Columns in Table XI, we show statistics of calibrations using only one tipping data pair taken only from one side. The results are similar to those listed in Table X. To reduce the calibration uncertainties, several techniques may be applied. One of them is to use tipping data from both sides. This technique depends on the fact that when a radiometer views the sky at angles θ and $180-\theta$, it sees opposite effects if a horizontal gradient is present. If we use the concept of normalized brightness temperatures, the observed normalized brightness temperatures at the two angles often differ from the zenith brightness temperature by opposite signs. Thus, some cancellation occurs, which reduces the calibration error. These error reductions are shown in the B Columns in Table XI.

Also shown in Table XI are performances of tipping calibration using different airmass pairs. The differences using different airmass pairs are not significant. To see the reason, we calculated the differences between the two normalized brightness temperatures at the listed airmass pairs on one side. Note that the magnitude of the difference reflects the degree of the horizontal inhomogeneity. The differences are then plotted against the calibration accuracies, shown in Fig. 7. It is observed that first, the calibration error almost linearly increases with the magnitude of the difference. Second, for the same value of the difference, the use of larger airmass yields smaller errors due to the larger separation of the brightness temperatures at the zenith and the off-zenith angle. Third, there are more points with large normalized brightness temperature differences when using large airmasses than those when using small airmasses. Thus, on average, the net effects of using different airmass pairs are about the same in the range of the airmass shown in the table.

The second technique to improve calibration accuracy is time averaging of the calibration factors. The effects of time averaging are shown in Table XII, in which we separated the data according to the dates when the lidar data were taken. Calibrations are performed using tipping data at airmass 1 and 2 on both sides. Column A, B, and C are corresponding to calibration accuracies with no 1-h and 3-h time averaging, respectively. We

Authorized licensed use limited to: Susanne Crewell. Downloaded on March 29, 2009 at 09:05 from IEEE Xplore. Restrictions apply.

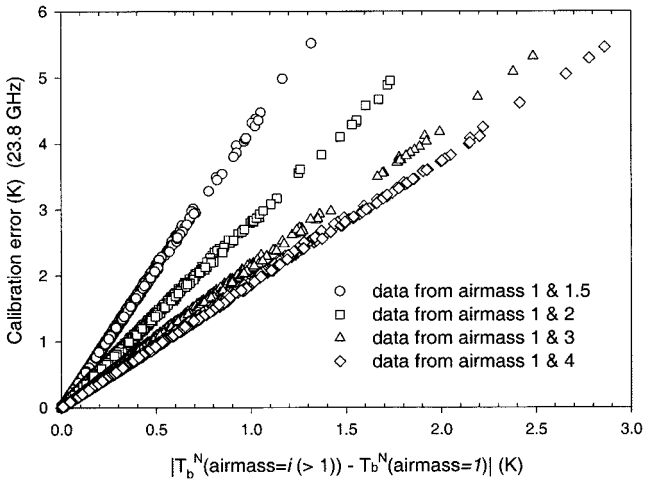

Fig. 7. Rms calibration errors as a function of the difference of two normalized brightness temperature measurements taken at two different airmasses. The figure also shows the dependence of the calibration errors on the airmasses at which the tipping observations are taken and used in the calibrations. The measurements are simulated from Raman lidar water vapor profiles.

see that the calibration errors are significantly reduced by this technique.

A third improvement is to screen the tipping data before applying them to the calibrations. We may select or reject tipping data by examining the standard deviation of the normalized brightness temperatures or the opacity-airmass correlation coefficient [7]. As an example, using a threshold of 0.4 K of the standard deviation to screen the data, on average, the calibration errors are reduced by about 10%.

V. Radiometer Calibration During WVIOP'97

During WVIOP'97, a number of *in situ* and remote water vapor sensors were operated together at the SGP CF, including two ETL and one ARM microwave radiometers, water vapor Raman lidars, two GPS systems, and radiosondes. All of the MWR's were calibrated using the tipping calibration method, but with two notable differences between ETL and ARM instruments. The ETL radiometers used airmasses 1, 2, and 3, while ARM used 1, 1.5, 2, 2.5, and 3. The ETL instruments performed tipping calibrations a few times a day for all of the clear days of the experiment, and the ARM radiometer performed tipping calibrations continuously for two days during the experiment with no other tipping calibrations being taken. Intercomparisons of data from these sensors revealed that the ARM radiometer measured PWV during this period about 1 to 2 mm higher than that from other sensors.

During the experiment, the ARM's radiometer collected two sets of time series of tipping measurements, each about 24 h. In the series, each tipping data unit contains ten measurements at elevation angles with airmasses 1, 1.5, 2, 2.5, and 3 on both sides. The ten measurements were completed every one minute. We first derived two sets of time series of the calibration factors using tipping data from each of the two sides. The two series were then compared to see if the instrument was properly leveled. Unfortunately, a significant bias existed between the two sets of calibration factors, which could not be explained by the horizontal inhomogeneity. It was later found that the elevation angles were shifted by a constant value. We estimated the amount of shift by adjusting the values of the elevation angles until the two sets of factor time series agreed. The angular shift was determined to be 1.3°. Although, as discussed in Section IV-C, this shift has little direct impact on the calibrations, provided that tipping data from both sides are used, the indirect impact is significant because a large number of useful tipping data are rejected by a quality control algorithm that checks the symmetry of the tipping data taken at symmetric angles.

With the corrections of the elevation angles and the applications of all the techniques discussed in previous sections, the values of PWV are reduced by about 0.5 mm. The reduction is largely due to the antenna beam width corrections that were not included in the original system calibrations and the radiometer pointing angle correction.

To explain the remaining PWV bias, we examined the calibration processes by comparing the time series of calibration factors that were derived at airmass pairs (1, 1.5), (1, 2), (1, 2.5), or (1, 3). We expect that the four time series of the calibration factors should have zero biases between any two of them. Significant biases imply problems in the calibration process. Such a problem could be a constant horizontal gradient of water vapor field, additional errors in pointing angles, or an antenna beam that picks up unexpected radiation when it points at lower elevation angles. Such consistent biases do exist in the data from the ARM radiometer system as shown in Fig. 8, where open circles are the calibration factors derived from data from airmasses 1 and 1.5 while the filled triangles are those from airmasses 1 and 2. The biases exist over the entire experiment. The causes of these biases are still under investigation. But the presence of these biases clearly violates the principle of the tipping calibrations.

VI. Discussion and Conclusions

The tipping calibration method derives a calibration factor from a set of brightness temperature measurements at two or more observation angles. The process requires a knowledge of the fundamental relationship between the airmass and the observation angle. This relationship may be modeled by (28) under stratified sky conditions. Horizontal inhomogeneity of the water vapor and temperature fields causes uncertainties in the relationship. The method also requires a mapping of the brightness temperature into the opacity with an estimated parameter, mean radiating temperature T_{mr}. The mapping uncertainty becomes larger when mapping a larger brightness temperature. For this reason, the tipping calibration technique is usually not applicable to a radiometer at a frequency with large optical depth unless T_{mr} error can be reduced. Other sources we have discussed that cause calibration uncertainties include earth curvature, antenna beam width, and radiometer pointing angle errors. For each of the sources, we have developed techniques to reduce its negative effect.

Neglecting earth curvature may cause a 0.1° of calibration error. The effect can be reduced to a negligible level by using (28). Without a correction, a 6° antenna beam width may cause about a 0.5° K of calibration error. For an antenna power pat-

Authorized licensed use limited to: Susanne Crewell. Downloaded on March 29, 2009 at 09:05 from IEEE Xplore. Restrictions apply.

TABLE XII
RMS CALIBRATION ERRORS (K) USING TIPPING DATA AT AIRMASS 1 AND 2 ON BOTH SIDES. COLUMNS A: CALIBRATION WITHOUT TIME AVERAGING, COLUMNS B: 1 h AVERAGE OF CALIBRATION FACTORS, COLUMNS C: 3 h AVERAGE OF CALIBRATION FACTORS. ROWS a, b, c, d, AND e CORRESPOND TO SEPTEMBER 26, 27, 29, 30 AND OCTOBER 1, 1997, RESPECTIVELY

	20.6 GHz			22.235 GHz			23.8 GHz			31.4 GHz		
	A	B	C	A	B	C	A	B	C	A	B	C
a	0.29	0.08	0.03	0.44	0.14	0.06	0.38	0.11	0.04	0.21	0.04	0.03
b	0.36	0.08	0.01	0.59	0.18	0.02	0.48	0.12	0.02	0.20	0.06	0.05
c	0.28	0.04	0.03	0.43	0.07	0.05	0.37	0.07	0.05	0.20	0.07	0.06
d	0.56	0.15	0.14	0.94	0.29	0.28	0.74	0.21	0.20	0.35	0.07	0.06
e	0.61	0.15	0.07	0.99	0.26	0.12	0.8	0.21	0.09	0.30	0.07	0.04

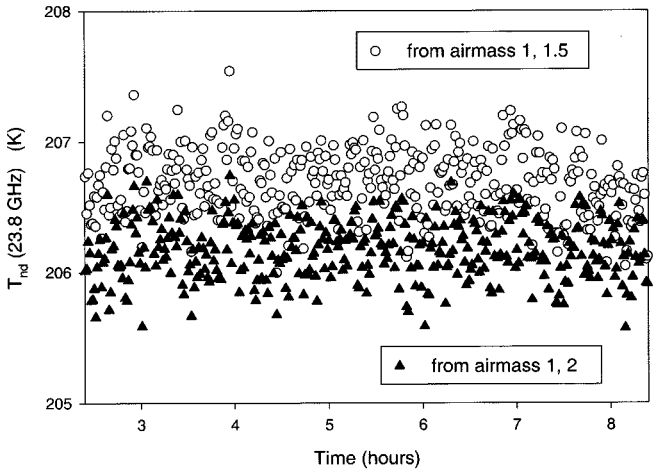

Fig. 8. Time series of noise injection temperatures, related to calibration factor by (16) and (17), derived from tipping data pairs at airmasses 1 and 1.5 (open circles), or airmasses 1 and 2 (filled triangles).

tern that can be approximated by a Gaussian function, (30) can be used to reduce the error to a few hundredths of a degree. Another method of reducing this effect was pointed out by an anonymous reviewer and in this method, the observation angles of the antenna are effectively shifted (downward) to compensate for the beam width effect. This shift needs to be determined only once for a given antenna pattern. The benefit of this approach is that the correction does not depend on the opacity. Although we agree that the angle shift method has merit, an evaluation and comparison with the present method was beyond the scope of our work. The uses of climatological means of T_{mr} result in calibrations with errors up to about 0.5°. The errors can be reduced to about 0.1° if the surface temperature is used to predict T_{mr}. The radiometer pointing angle errors can cause large uncertainties in calibrations: about 2° of calibration errors result from 1° point error. Fortunately, uncertainties caused by 1° pointing error can often be reduced to about 0.1° if tipping data on both sides are used. The horizontal inhomogeneity is another source that potentially could cause large uncertainties in the calibrations. These uncertainties can be reduced by performing time averaging and spatial averaging (using tipping data from both sides). If there is no consistent horizontal gradient, the averaging technique should reduce the calibration uncertainties to a few tenths of a degree as we demonstrated using simulated tipping data from Raman lidars. Thus, we expect that the tipping calibration technique may provide calibration accuracy of about 0.5°.

We have shown that calibrations using low elevation angles are more sensitive to the various error sources. However, *for the same error*, angles with larger separations give a mathematical advantage in least squares estimation. Thus, there is clearly a tradeoff on the choice of angles. From our experience and the earlier discussions, tipping data should not include airmass greater than 3, especially for antenna with beamwidths $\geq 6°$.

The tipping data quality control techniques are also useful in reducing calibration errors. The technique of checking the symmetry of the tipping data taken at symmetric angles can be used to ensure a stratified atmosphere, or the correctness of system pointing angles. The standard deviation of normalized brightness temperature measurements, or airmass-opacity correlation coefficient [7] can be used to screen out erroneous tipping data. The comparisons of calibration factors derived from different combinations of airmasses can be used to check the overall performance of the calibrations.

There have been questions as to whether or not multiple calibration factors in a radiometer equation can be derived from the tipping data. From our experience, it is difficult to derive even two constant factors from a single realization of an atmospheric state. Theoretically, determining multiple factors depends on multiple sets of tipping calibrations that are obtained in various atmospheric states with different water vapor contents. However, the various uncertainties discussed earlier often cause the numerical solutions to be unstable. Thus, it is often better to determine one factor and estimate the remaining factors using other means, such as theoretical calculations, target calibration, or radiosonde (with RTE model) calibrations. However, calibration with a RTE model is unacceptable if one is trying to study absorption and radiative processes.

As our investigation progressed, it became clear that there were significant advantages to having nearly continuous tipping calibrations. The presence of significant horizontal inhomogeneities as they pass overhead is easily revealed by a time series of tipping calibration data. If these tipping data are done frequently and in clear conditions, a representative time series of zenith T_b is still obtained. During cloudy conditions, the off-zenith scans can be used to identify cloudy data that are not necessarily overhead. This is important because cloud

Authorized licensed use limited to: Susanne Crewell. Downloaded on March 29, 2009 at 09:05 from IEEE Xplore. Restrictions apply.

ceilometers or FTIR's usually only indicate clear conditions in the zenith direction. A large initial data set is also advantageous when applying rigorous quality control methods. For example, ARM radiometer, with its continuous scanning ability, generated roughly 3000 1-min tipping calibration scans; during the same period, the ETL radiometers generated only about 30 15-min scans.

In this investigation, we have assumed a linear radiometric system. In reality, however, this assumption may not be completely valid. Although it is difficult to evaluate such situations, problems can often be identified by using strict quality control techniques of tipping data.

APPENDIX

The antenna temperature T_A at an elevation and azimuthal angles (θ, φ) may be calculated as [18]

$$T_A(\theta, \varphi) = \frac{\int_0^{2\pi}\int_0^{\pi} P(\theta, \varphi; \eta', \xi') T_b(\eta', \xi') \sin(\eta')\, d\eta'\, d\xi'}{\int_0^{2\pi}\int_0^{\pi} P(\theta, \varphi; \eta', \xi') \sin(\eta')\, d\eta'\, d\xi'} \tag{A1}$$

where P is the antenna power pattern, and T_b is the sky brightness temperature at the direction $\boldsymbol{k}$. T_b has a polar angle η' and an azimuth angle ξ' in the $X'Y'Z'$ Cartesian coordinate system and polar and azimuth angles η, ξ in the XYZ system. In the $X'Y'Z'$ system, the radiometer is located at the origin and pointed in the direction of the Z' axis. The Z' axis has an angle β with the Z coordinate in the XYZ Cartesian coordinate system. In the XYZ system, the Z axis points at the zenith direction and the X axis coincides with the X' axis of the $X'Y'Z'$ system. The angle $\theta = \pi/2 - \beta$ is the elevation or observation angle. We assume a Gaussian gain pattern as

$$P = \exp(-\eta'^2/2\sigma^2). \tag{A2}$$

The parameter σ is related to the antenna beam width as

$$\sigma = \frac{\theta_{1/2}}{2\sqrt{2\mathrm{Ln}(2)}} \tag{A3}$$

where $\theta_{1/2}$ is the full width at half-maximum power of the power pattern in radians.

Using (13), we may write T_b in the XYZ system as

$$T_b(\eta) = T_{mr} - (T_{mr} - T_{bb}) \exp(-\tau(\eta)) \tag{A4}$$

where τ is the slant path opacity at the zenith angle η and may be written by using (27)

$$\tau(\eta) = \tau_0 \left[\mu_\eta^{-1} - H\mu_\eta^{-1}(\mu_\eta^{-2} - 1)/r_e\right] \tag{A5}$$

where τ_0 is the zenith opacity, and $\mu_\eta = \cos(\eta)$. The mean radiating temperature T_{mr} is assumed independent from elevation angles because its variation with angles is small, as is shown in Table VII(a). Using the angle relationship

$$\mu_\eta = \mu_\eta(\eta', \xi') = \sin(\beta)\sin(\eta')\sin(\xi') + \cos(\beta)\cos(\eta') \tag{A6}$$

we may expand μ_η to second order with respect to η' around $\eta' = 0$, and get

$$\mu_\eta \approx \mu_\beta + \sin(\beta)\sin(\xi')\eta' - \frac{\mu_\beta}{2}\eta'^2 \tag{A7}$$

where $\mu_\beta = \mu(0, \xi') = \cos(\beta)$. We may also expand T_b to second order with respect to μ_η at μ_β in the $X'Y'Z'$ system in the form

$$T_b(\mu_\eta) \approx T_b(\mu_\beta) + \left.\frac{dT_b}{d\mu_\eta}\right|_{\mu_\beta} (\mu_\eta - \mu_\beta) + \frac{1}{2}\left.\frac{d^2T_b}{d^2\mu_\eta}\right|_{\mu_\beta} (\mu_\eta - \mu_\beta)^2. \tag{A8}$$

Using (A4), (A5), (A7), and (A8), we have

$$T_b(\eta', \xi') = T_b(\beta) - (T_{mr} - T_{bb}) e^{-\tau_0(\mu_\beta^{-1} - \Delta_0)} \cdot \tau_0 [(\mu_\beta^{-2} + \Delta_1)\sin(\beta)\sin(\xi')\eta' - \tfrac{1}{2}b\eta'^2 + \cdots] \tag{A9}$$

where

$$\Delta_0 = \frac{H}{r_e}\mu_\beta^{-1}(\mu_\beta^{-2} - 1) \tag{A10}$$

$$b = \mu_\beta^{-1} + \Delta_1\mu_\beta + \left[-\tau_0(\mu_\beta^{-2} + \Delta_1)^2 + 2\mu_\beta^{-3} - \Delta_2\right] \cdot \sin^2(\beta)\sin^2(\xi')$$

$$\Delta_1 = \frac{H}{r_e}\mu_\beta^{-2}(1 - 3\mu_\beta^{-2}) \tag{A11}$$

and

$$\Delta_2 = \frac{H}{r_e}\mu_\beta^{-3}(12\mu_\beta^{-2} - 2). \tag{A12}$$

Substitute (A2) and (A9), neglecting the fourth-order term, into (A1), and noting $\beta = \pi/2 - \theta$, the integral yields the result

$$\Delta T_A(\theta) = \frac{\theta_{1/2}^2}{16\mathrm{Ln}(2)}(T_{mr} - T_{bb})\exp(-\tau)\left\{2(1 + \Delta_1\mu_\beta^2) + \left[2 - \frac{(1 + \Delta_1\mu_\beta^2)^2}{1 - \Delta_0\mu_\beta}\tau - \Delta_2\mu_\beta^3\right]\frac{\cos^2(\theta)}{\sin^2(\theta)}\right\} \cdot \frac{\tau}{1 - \Delta_0\mu_\beta}. \tag{A13}$$

In (A13), the terms involving $\boldsymbol{\Delta}_0$, $\boldsymbol{\Delta}_1$, and $\boldsymbol{\Delta}_2$ are related to the earth curvature effect. Their contributions to the brightness temperature correction is less than 2% in the airmass range 1–4. If we neglect these terms, we obtain (30).

ACKNOWLEDGMENT

The authors would like to thank D. Hazen for assistance in deploying the ETL microwave radiometers, J. Liljegren, and S. Clough for discussions on tipping calibration, and D. Whiteman and D. Turner for providing the Raman lidar data used in our study. The authors would also like to thank the four anonymous reviewers, especially reviewer number three, for their useful comments to the original manuscript.

REFERENCES

[1] S. A. Clough, "The water vapor continuum and its role in remote sensing," *Opt. Remote Sensing Atmos.*, vol. 2, pp. 76–78, 1995.

[2] J. R. Eyre, G. A. Kelly, A. P. McNally, E. Anderson, and A. Persson, "Assimilation of TOVS radiance information through one-dimensional variational analysis," *Quart. J. Roy. Meteorol. Soc.*, vol. 119, pp. 1427–1463, 1993.

[3] H. E. Revercomb, H. Buijs, H. B. Howell, D. D. LaPorte, W. L. Smith, and L. A. Sromovsky, "Radiometric calibration of IR Fourier transform spectrometers: Solution to a proble with the high-resolution interferometer sounder," *Appl. Opt.*, vol. 27, pp. 3210–3218, 1988.

Authorized licensed use limited to: Susanne Crewell. Downloaded on March 29, 2009 at 09:05 from IEEE Xplore. Restrictions apply.

[4] Y. Han, J. A. Shaw, J. H. Churnside, P. D. Brown, and S. A. Clough, "Infrared spectral measurements in the tropical Pacific atmosphere," *J. Geophys. Res.*, vol. 102, pp. 4353–4356, 1997.
[5] G. M. Stokes and S. E. Schwartz, "The atmospheric radiation measurement (ARM) program: Programmatic background and design of the cloud and radiation testbed," *Bull. Amer. Meteorol. Soc.*, vol. 75, pp. 1201–1221, 1994.
[6] J. C. Liljegren and B. M. Lesht, "Measurements of integrated water vapor and cloud liquid water from microwave radiometers at the DOE ARM cloud and radiation testbed in the U.S. Southern Great Plains," in *Proc. IGARSS'96*, Lincoln, NE, 1996, pp. 1675–1677.
[7] ——, "Two-channel microwave radiometer for observations of total column precipitable water vapor and cloud liquid water path," in *Proc. 5th Symp. Global Change Studies*, Nashville, TN, Jan. 23–28, 1994, pp. 262–269.
[8] E. R. Westwater, "Ground-based microwave remote sensing of meteorological variables," in *Atmospheric Remote Sensing by Microwave Radiometry*, M. Janssen, Ed. New York: Wiley, 1993.
[9] J. Askne and E. R. Westwater, "A review of ground-based remote sensing of temperature and moisture by passive microwave radiometers," *IEEE Trans. Geosci. Remote Sensing*, vol. GE-24, pp. 340–352, May 1986.
[10] E. R. Westwater, "The accuracy of water vapor and cloud liquid determination by dual-frequency ground-based microwave radiometry," *Radio Sci.*, vol. 13, pp. 667–685, 1978.
[11] J. Duan *et al.*, "GPS meteorology: Direct estimation of the absolute value of precipitable water," *J. Appl. Meteorol.*, vol. 35, pp. 830–838, 1996.
[12] S. A. Clough *et al.*, "Implications for atmospheric state specification from the AERI/LBLRTM quality measurement experiment and the MWR/LBLRTM quality measurement experiment," in *Proc. 6th Atmospheric Radiation Measurement (ARM) Science Team Meeting*, San Antonio, TX, Mar. 4–7, 1996, pp. 45–49.
[13] J. P. Hollinger, J. L. Pierce, and G. A. Poe, "SSM/I instrument evaluation," *IEEE Trans. Geosci. Remote Sensing*, vol. 28, pp. 781–790, Sept. 1990.
[14] Y. Han, J. B. Snider, E. R. Westwater, S. H. Melfi, and R. A. Ferrare, "Observations of water vapor by ground-based microwave radiometers and Raman lidar," *J. Geophys. Res.*, vol. 99, pp. 18 695–18 702, 1994.
[15] D. C. Hogg, F. O. Guiraud, J. B. Snider, M. T. Decker , and E. R. Westwater, "A steerable dual-channel microwave radiometer for measurement of water vapor and liquid in the troposphere," *J. Appl. Meteorol.*, vol. 22, pp. 789–806, 1983.
[16] M. A. Janssen, "An introduction to the passive microwave remote sensing of atmospheres," in *Atmospheric Remote Sensing by Microwave Radiometry*, M. Janssen, Ed. New York: Wiley, 1993.
[17] A. Stogryn, "A note on brightness temperature at millimeter wavelengths," *IEEE Trans. Geosci. Electron.*, vol. GE-13, no. 2, pp. 81–84, 1975.
[18] F. T. Ulaby, R. K. Moore, and A. K. Fung, *Microwave Remote Sensing, Active and Passive, Volume I, Microwave Remote Sensing Fundamentals and Radiometry*. Reading, MA: Addison-Wesley, 1981.
[19] M. T. Decker and J. A. Schroeder, "Calibration of ground-based microwave radiometers for atmospheric remote sensing,", Boulder, CO, NOAA Tech. Mem., ERL WPL-197, 1991.
[20] J. B. Snider and D. A. Hazen, "Surface-based radiometric observations of water vapor and cloud liquid in the temperate zone and in the tropics," *Radio Sci.*, vol. 33, pp. 421–432, 1998.
[21] E. R. Westwater, J. B. Snider, and M. J. Falls, "Ground-based radiometric observations of atmospheric emission and attenuation at 20.6, 31.65, and 90 GHz: A comparison of measurements and theory," *IEEE Trans. Antennas Propag.*, vol. AP-38, pp. 1569–1580, Oct. 1990.
[22] J. A. Schroeder and E. R. Westwater, "Users' guide to WPL microwave radiative transfer software,", Boulder, CO, NOAA Tech. Memo., ERL-WPL 213, 1991.
[23] B. R. Bean and E. J. Dutton, *Radio Meteorology*. New York: Dover, 1968.
[24] C. Dragone, "Characteristics of a broadband microwave corrugated horn: A comparison between theory and experiment," *Bell Syst. Tech. J.*, vol. 56, no. 6, pp. 869–888, 1997.
[25] E. R. Westwater, Y. Han, V. G. Irisov, V. Y. Leuskiy, Y. G. Trokhimovski, C. W. Fairall, and A. T. Jessup, "Sea-air and boundary layer temperature measured by a scanning 5-mm-wavelength radiometer: Recent results," *Radio Sci.*, vol. 33, pp. 291–302, 1998.
[26] B. E. Martner, D. B. Wuertz, B. B. Stankov, R. G. Strauch, E. R. Westwater, K. S. Gage, W. L. Ecklund, C. L. Martin, and W. F. Dabberdt, "An evaluation of wind profiler, RASS, and microwave radiometer performance," *Bull. Amer. Meteorol. Soc.*, vol. 74, pp. 599–616, 1993.
[27] S. H. Melfi and D. Whiteman, "Observation of lower atmospheric moisture structure and its evolution using a Raman lidar," *Bull. Amer. Meterol.*, vol. 28, pp. 789–806, 1985.
[28] D. N. Whiteman, S. H. Melfi, and R. A. Ferrare, "Raman lidar system for the measurement of water vapor and aerosols in the Earth's atmosphere," *Appl. Opt.*, vol. 31, pp. 3068–3082, 1992.
[29] J. E. M. Goldsmith, F. H. Blair, S. E. Bisson, and D. D. Turner, "Turn-key Raman lidar for profiling atmospheric water vapor clouds and aerosols," *Appl. Opt.*, vol. 37, pp. 4979–4990, 1998.

Yong Han was born in China. He received the B.S. degree in 1982 and the M.S. degree in 1985 in meteorology from the Nanjing Institute of Meteorology, Nanjing, China. In 1992, he received the Ph.D. degree in meteorology from the Pennsylvania State University, University Park.

He was awarded a Postdoctoral Research Associateship by the National Research Council from 1992 to 1994. Since 1994, he has been with the University of Colorado, Cooperative Institute for Research in the Environmental Sciences (CIRES), Boulder, working at the NOAA/Environmental Technology Laboratory on remote sensing of atmosphere and ocean surface using both passive and active sensors.

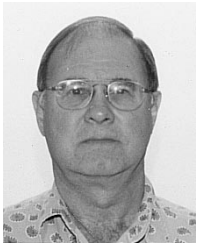

Ed R. Westwater (SM'91) was born in Denver, CO, in 1937. He received the B.A. degree in physics and mathematics from Western State College of Colorado, Gunnison, in 1959, and the M.S. and Ph.D. degrees in physics from the University of Colorado, Boulder, in 1962 and 1970, respectively.

He is currently a Research Associate with the Cooperative Institute for Research in the Environmental Sciences (CIRES), University of Colorado/National Oceanic and Atmospheric Administration (NOAA), Boulder, and is associated with the Ocean Remote Sensing Division of Environmental Technology Laboratory, NOAA, Boulder. He was with the U.S. Department of Commerce from 1960 to 1995 and joined CIRES in 1995. His research has been concerned with microwave absorption in the atmosphere, remote sensing of the ocean surface, microwave and infrared radiative transfer, ground- and satellite-based remote sensing by passive radiometry, and the application of mathematical inversion techniques to problems in remote sensing.

Authorized licensed use limited to: Susanne Crewell. Downloaded on March 29, 2009 at 09:05 from IEEE Xplore. Restrictions apply.